Check for updates

Wiley
International Journal of Energy Research
Volume 2025, Article ID 5520837, 16 pages
https://doi.org/10.1155/er/5520837

WILEY

*Research Article*

# Framework-Guided Synthesis of Zinc Ferrite for Lithium-Ion Battery Application

**Thirumalaisamy Kiruthika,[1] Devaraj Lakshmi,[2] Seung Jo Yoo,[3] Zungsun Choi,[4] Pachagounder Sakthivel,[5] Jun Young Cheong,[6] Byungil Hwang,[7] and Paneerselvam Christopher Selvin[1]**

[1]*Department of Physics, Bharathiar University, Coimbatore, Tamil Nadu 46, India*
[2]*Department of Physics, PSG College of Arts and Science, Coimbatore, Tamil Nadu 14, India*
[3]*Research Center for Materials Analysis, Korea Basic Science Institute (KBSI), Daejeon, Republic of Korea*
[4]*School of Creative Convergence Education, Handong Global University, Pohang 37554, Republic of Korea*
[5]*Department of Nanoscience and Technology, Bharathiar University, Coimbatore, Tamil Nadu 43, India*
[6]*James Watt School of Engineering, University of Glasgow, Glasgow, G12 8QQ, UK*
[7]*School of Integrative Engineering, Chung-Ang University, Seoul 06974, Republic of Korea*

Correspondence should be addressed to Jun Young Cheong; junyoung.cheong@glasgow.ac.uk, Byungil Hwang; bihwang@cau.ac.kr, and Paneerselvam Christopher Selvin; csphysics@buc.edu.in

Received 12 August 2024; Accepted 11 March 2025

Academic Editor: Vinayak Parale

Copyright © 2025 Thirumalaisamy Kiruthika et al. International Journal of Energy Research published by John Wiley & Sons Ltd. This is an open access article under the terms of the Creative Commons Attribution License, which permits use, distribution and reproduction in any medium, provided the original work is properly cited.

Spinel zinc ferrite ($ZnFe_2O_4$) (ZFO) nanomaterials were prepared as anodes for lithium-ion batteries (LIBs) using ice crystals and Triton X-100 as the hard and soft templates, respectively, via the sol–gel method. This novel, facile, energy-efficient, and economical approach yields ZFO nanoparticles with controlled morphology and homogeneous grain distribution. The crystallinity of the ZFO samples was confirmed by X-ray diffraction (XRD); the crystallite sizes of the prepared samples were found to be 20 and 23 nm for the ice- and soft-templated ZFO samples, respectively. A spherical morphology was achieved using both templates although the soft-templated sample underwent agglomeration unlike the hard-templated sample. Similar elemental composition was achieved for the samples using both methods, as observed by energy-dispersive X-ray spectroscopy. The ZFO electrodes exhibited excellent electrochemical performance in nonaqueous systems, displaying a distinctive pair of reversible redox peaks for 50 cycles. The hard-templated (ice crystal) ZFO anode demonstrated an excellent capacity retention of 89.30%, an average Coulombic efficiency of 99.67%, and a final discharge capacity of 793.00 mAh $g^{-1}$ over 500 cycles at 0.5 A $g^{-1}$. In contrast, the soft-templated (Triton X-100) ZFO anode delivered a capacity retention of 73.02%, an average Coulombic efficiency of 98.40%, and a final discharge capacity of 625.00 mAh $g^{-1}$ over 500 cycles under the same conditions. Our findings highlight those hard-templated methods, such as ice crystal template, can significantly enhance the electrochemical properties and performance of metal oxide–based electrode materials for LIBs. This improvement is achieved through precise control of morphology, grain distribution, phase purity, and crystal structure. Additionally, hard-templated method can be a stand-alone technique for the commercial mass production of metal oxide–based electrode materials owing to its reliable, facile, and economical nature.

**Keywords:** anode; capacity; Coulombic efficiency; ice-template synthesis; Li-ion batteries; soft template; spinel zinc ferrite

## Summary

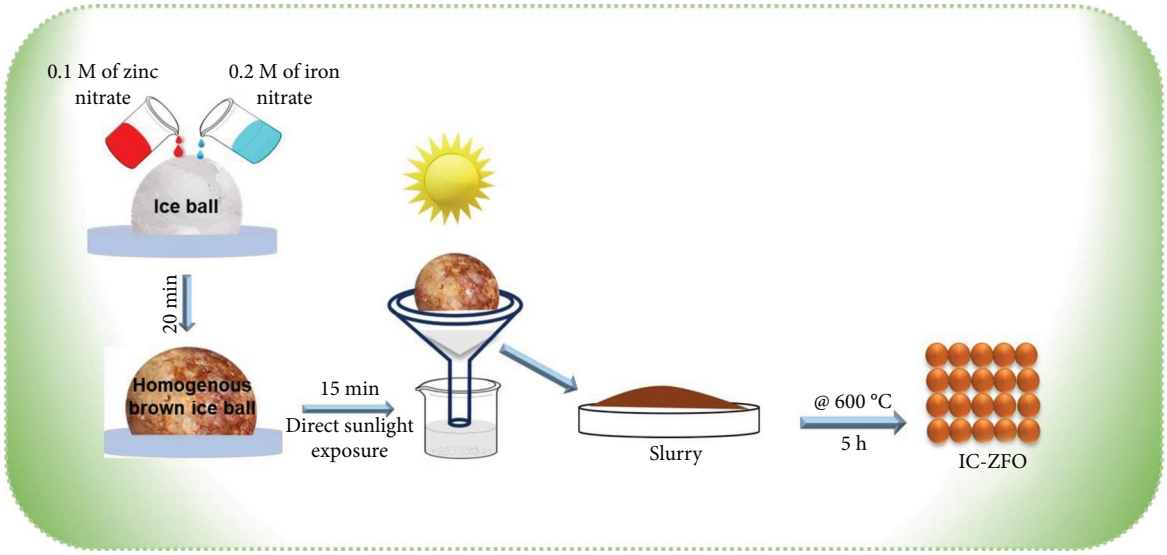
- The spinel zinc ferrite ($ZnFe_2O_4$) (ZFO) nanoparticles were synthesized using a rapid ice-template method (IC-ZFO) and sol–gel method with Triton X-100 (S-ZFO).
- IC-ZFO demonstrates superior electrochemical performance: 797/793 mAh $g^{-1}$ capacity and 99.4% Coulombic efficiency at the 500th cycles.
- Triton X-100 ZFO (S-ZFO) anodes show 674/625 mAh $g^{-1}$ capacity and 92.7% Coulombic efficiency at 500th cycles
- Grain distribution significantly impacts anodic properties, affecting charge transfer kinetics and grain boundary contributions. Ice template synthesis yields uniform morphology and small crystallite sizes, enhancing charge transfer and ion diffusion.

## 1. Introduction

In recent years, the demand for high-performance lithium-ion batteries (LIBs) has been growing in various industries. Thus, battery components, especially electrodes, must be upgraded and explored to achieve enhanced energy and power densities, prolonged cycle life, and affordability [1–3]. An anode is a crucial component in a battery, governing the energy density, discharge capacity, and stability of the system. Despite immense growth and research in the development of high-performance anodes, an efficient anode and thus a suitable battery remain unexplored [4–7]. The choice of the anode material plays a significant role in improving battery performance and cycle life. Commercial graphite anodes for LIBs exhibit low theoretical capacity (~372 mAh $g^{-1}$) and cannot meet the requirements of high-energy applications. As an alternative, transition metal oxides (TMOs) such as $SnO_2$, ZnO, $TiO_2$, and $SiO_2$ along with specific structures such as perovskites and rutile have emerged as promising anode materials for LIBs [8–10]. In particular, binary TMOs, such as lithium titanate, doped rock salt–type structures, and $AB_2O_4$ structures, have attracted considerable attention in various fields owing to their excellent electrochemical, catalytic, and magnetic properties and high theoretical capacities based on conversion reactions [11–13]. Particularly, spinel zinc ferrite ($ZnFe_2O_4$) (ZFO) outperforms other combinations of TMOs owing to its exceptional properties, such as high theoretical capacity (1072 mAh $g^{-1}$), low toxicity, abundant resources, and low working voltage (~1.5 V for Li extraction) [14, 15]. However, ZFO exhibits low electrical conductivity, undergoes volume changes during cycling, and has electrolyte compatibility issues, all of which are associated with the intrinsic aspects of the material. Hence, an optimized synthesis process can address issues such as ordered morphology, phase purity, and other factors that enable ZFO to exhibit its full potential as an anode [16–18]. Spinel ZFO nanoparticles were prepared using different synthetic routes. Generally, the rate of the chemical reaction depends on various factors such as calcination temperature, pressure, pH, complexing agents, and synthesis time. The particle size can be controlled using various strategies that require heating the reaction mixtures. These strategies include hydrothermal [19], coprecipitation [20], sol–gel [21], chemical bath deposition (CBD) [22], solvothermal [23], spray pyrolysis [24], and chemical vapor deposition synthesis at high calcination temperatures [25]. The common chemical synthesis methods, such as sol–gel, coprecipitation, hydrothermal, solid-state reactions, and spray pyrolysis, have several drawbacks. They often require high energy, lengthy processing times, and expensive equipment. Achieving consistent particle morphology is challenging, and impurities can affect material performance. Additionally, the use of hazardous solvents raises environmental concerns, limiting sustainability [26, 27]. The morphological and textural properties of metal oxides can be controlled using soft/hard templates, growth directing agents, surfactants, and capping agents. Current research on ZFO nanoparticles focuses on synthesis methods such as CBD and dip coating [28]. However, these methods typically require long reaction times (~15 h) to obtain pristine and uniform nanoparticles. Additionally, variations in temperature during synthesis can lead to the formation of agglomerated and inhomogeneous nanoparticles. For instance, the sol–gel process involves stirring at 80°C, drying the formed gel at 120°C in a hot air oven, and calcining the dried gel at 600°C in a furnace to form a pure-phase nanomaterial. To address these issues and explore strategies other than the conventional wet chemical methods, an alternative rapid precipitation method at room temperature (27°C) is essential for preparing uniform nanostructures of ZFO with abundant voids, which can enhance the overall performance of LIBs. To address these limitations, this study introduces a novel ice-template (hard-templated) method, which is eco-friendly, cost-effective, and energy-efficient. Unlike conventional soft-templated methods, ice-template [17, 23] allows precise control over the morphology and porosity of ZFO nanoparticles. This self-organizing approach ensures enhanced crystallinity, homogeneous grain distribution, and the formation of a hierarchically porous structure, which collectively improve lithium-ion transport and structural stability [29, 30]. Previous research works [31] shows ZFO anode synthesized via ice-template exhibits superior electrochemical performance, including excellent capacity retention, high Coulombic efficiency, and prolonged cycling stability. Furthermore, a comprehensive comparison with soft template (using Triton X-100) clearly demonstrates the advantages of the ice-template method in enhancing zinc ferrite performance. By optimizing the synthesis route and addressing structural and morphological issues, this work successfully unlocks the full potential of ZFO as a high-performance anode material. Compared to hydrothermal or solvothermal methods, ice-template is less complex, uses readily available materials, and eliminates the need for high-pressure conditions or specialized equipment, making it a practical and efficient choice for high-performance nanomaterials [23].

In this study, an effective method for the rapid synthesis of ZFO nanoparticles using ice crystals to self-control their morphology during the process is proposed. The study also involves a comparison of the proposed ice-template-assisted approach with the traditional soft-templated method (the corresponding spinel ZFO is denoted as S-ZFO). As mentioned above, the small change in the synthesis of ZFO via

ijer, 2025, 1, Downloaded from https://onlinelibrary.wiley.com/doi/10.1155/er/5520837 by Chung-Ang University, Seoul, Wiley Online Library on [06/05/2025]. See the Terms and Conditions (https://onlinelibrary.wiley.com/terms-and-conditions) on Wiley Online Library for rules of use; OA articles are governed by the applicable Creative Commons License




Scheme 1: Schematic of the ice-template synthesis.

the proposed method alters the morphology and consequently affects its physicochemical and electrochemical performance; the corresponding findings are also discussed. The findings presented here not only advance the understanding of morphology-controlled ZFO synthesis but also contribute to the broader development of scalable and sustainable LIB technologies. Compared to existing methods, the proposed ice-template approach is simpler, avoids harmful chemicals, and eliminates the need for complex equipment, making it suitable for commercial-scale production of high-performance metal oxide-based electrode materials.

## 2. Experimental

*2.1. Materials and Methods.* All required materials including zinc nitrate ($Zn(NO_3)_2 \cdot 6H_2O$), ferric nitrate ($Fe(NO_3)_2 \cdot 9H_2O$), Triton X-100 ($C_{34}H_{62}O_{11}$), and citric acid were utilized without further refinement, as they were of analytical grade. These materials were sourced from HiMedia, India, and had a purity of 99%.

*2.1.1. Ice-Template-Assisted Method.* The process for preparing ice-template-synthesized spinel ZFO (IC-ZFO) powder is illustrated in Scheme 1. $Zn(NO_3)_2 \cdot 6H_2O$ (0.2 M) and iron nitrate (0.1 M) were dissolved in 10 mL of distilled water. Once a clear solution was obtained, it was poured onto crushed ice balls. These precursor-loaded ice balls were then allowed to rest for 20 min to ensure the uniform distribution of the precursors, during which the initially white ice balls gradually turned brown, indicating the homogeneous dispersion of the precursors within the ice crystals. Subsequently, the brownish ice balls were removed from the refrigerator and placed in a funnel fitted with Whatman filter paper Grade 1. The funnel was placed under direct sunlight for 15 min, causing the ice balls to slowly melt into water while simultaneously filtering through the funnel. After the complete filtration of ice crystal water, the remaining brown precipitate was collected and dried for 5 min in hot air. Finally, IC-ZFO were obtained by annealing the precipitate at 600°C for 5 h.

*2.1.2. Surfactant-Assisted Method.* In the synthesis process of Triton X-100-included ZFO nanoparticles through the sol–gel method, 0.1 M of zinc nitrate, 0.2 M of $Fe(NO_3)_2 \cdot 9H_2O$, and citric acid were dissolved in 50 mL distilled water. The mixture was stirred vigorously for 3 h to obtain a homogeneous solution. The homogeneous solution underwent gel formation when heated to 80°C. The resulting gel was dried in a hot air oven at 120°C for 12 h to eliminate excess moisture. After drying, the powder was calcined at 600°C in a muffle furnace for 5 h to obtain the ZFO powder. For further incorporation of the surfactant into the ZFO nanoparticles, Triton X-100 was introduced into the mixture, which was maintained at 80°C. The mixture was transferred to an autoclave and heated at 100°C for 1 h in a hot air oven. The resulting precipitate was collected and purified by washing thrice with distilled water and ethanol.

*2.2. Characterization.* The crystal structure of the prepared spinel ZFO powders was confirmed by X-ray diffraction (XRD) conducted using a Philips X'Pert Pro diffractometer with Cu-Kα radiation (wavelength = 1.54 Å) over a 2θ range of 20°–70°. The morphology and size of the prepared ZFO samples were examined through field-emission scanning electron microscopy (FESEM) (Carl Zeiss model Sigma 300). Transmission electron microscopy (TEM) (Carl Zeiss, Libra 200 MC) was performed to clarify the structures and sizes of the as-prepared samples. The TEM analysis was conducted through the Korea Basic Science Institute in South Korea. The elemental composition of the prepared materials was confirmed through energy-dispersive spectroscopy (EDS). The vibrational peaks of the prepared material were observed through Fourier transform infrared (FTIR) spectroscopy in the range of 4000–400 $cm^{-1}$ using a Jasco Model 4100LE system with KBr-pressed pellets. Finally, the electrochemical performance of the prepared ZFO nanomaterials was evaluated through AC impedance and galvanostatic charging and discharging analyses and cyclic voltammetry (CV) at room temperature (27°C).

*2.2.1. Coin Cell Fabrication.* The electrochemical characterization of the samples was conducted using CR2016 coin cells,

ijer, 2025, 1, Downloaded from https://onlinelibrary.wiley.com/doi/10.1155/er/5520837 by Chung-Ang University, Seoul, Wiley Online Library on [06/05/2025]. See the Terms and Conditions (https://onlinelibrary.wiley.com/terms-and-conditions) on Wiley Online Library for rules of use; OA articles are governed by the applicable Creative Commons License

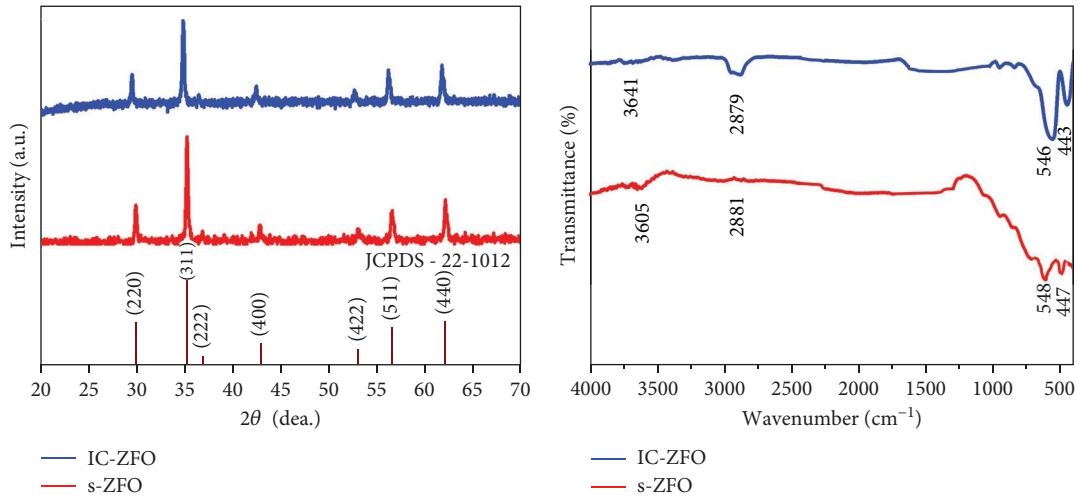



FIGURE 1: (a) XRD patterns of $ZnFe_2O_4$ nanoparticles confirming phase purity, with sharp peaks indicating good crystallinity and no impurity phases and (b) FTIR spectra of the prepared ZFO samples by hard-templated and soft-templated method.

TABLE 1: ZFO properties and impact on performance.

| Material | Crystallite size/particle size (nm) | Lattice constant (Å) | Volume (Å$^3$)/ strain (ε) | Charging/discharging capacity (mAh g$^{-1}$) | Coulombic efficiency (%) |
|---|---|---|---|---|---|
| IC-ZFO | 20/30 | 8.449 | 603.5/0.12 | 797/793 | 99.4 |
| S-ZFO | 23/40 | 8.383 | 593.8/0.16 | 674/625 | 92.7 |

with Li foil acting as the counter/reference electrode and a polypropylene film (Celgard 2400) as the separator. The working electrodes were prepared by coating a slurry composed of the active materials (ZFO), a conductive agent (Super P carbon black), and a binder (polyvinylidene difluoride) dispersed in the N-methyl pyrrolidone solvent onto a copper foil. Subsequently, the electrodes were dried in a vacuum oven for 12 h at 80°C, resulting in a mass loading of active materials of ~1.0 mg cm$^{-2}$. The coin cells were assembled in an Ar-filled glove box. The electrolyte utilized was 1 M $LiPF_6$ dissolved in a mixture of ethylene carbonate, dimethyl carbonate, and diethyl carbonate in a volume ratio of 1:1:1.

## 3. Results and Discussion

*3.1. Structural Analysis.* Figure 1a shows the XRD diffractogram of spinel ZFO prepared using the ice crystal and Triton X-100 templates. Well-defined and sharp diffraction peaks were observed in the XRD diffractogram of IC-ZFO. The observed diffraction peaks were indexed to JCPDS NO: 22-1012 [23]. Similarly, the XRD diffractogram of S-ZFO closely resembles that of IC-ZFO. Both patterns align perfectly with the cubic spinel structure characterized by the $Fd_3m$ space group. The crystallite sizes of the samples were determined using the Debye–Scherrer equation [5] to be ~20 nm for IC-ZFO and 23 nm for spinel S-ZFO. In addition, the XRD diffractogram can be used to determine the cation distribution in spinel ferrite. The distribution of divalent and trivalent cations in the octahedral and tetrahedral sites can be determined by the ratios of the XRD lines, specifically $I_{220}/I_{440}$ and $I_{422}/I_{400}$, as these planes are sensitive to cation distribution [32]. The peak intensities of the (220) and (440) planes are sensitive to the cations at the A sites, whereas the peak intensity of the (400) plane is sensitive to the cations at the B sites. The slight peak shift in the IC-ZFO material is observed in (311) plane. The shift in the (311) diffraction peak of IC-ZFO is attributed to the ice crystal synthesis method, which likely induces lattice expansion due to factors like defect incorporation, strain during freezing, or increased interplanar spacing promoted by uniform crystal growth in the ice matrix. Structural differences, such as changes in crystallite size and lattice constants, may also contribute to the shift. The XRD patterns of the ZFO samples indicated a strain of 0.12 for IC-ZFO and 0.16 for S-ZFO (Table 1). The lower strain observed for IC-ZFO suggests a more stable crystal structure, potentially reducing the number of defects and increasing electron transport efficiency, which can improve material performance [33]. Furthermore, although the lattice parameters were similar for both methods, the higher volume observed for IC-ZFO indicates a larger unit cell size, indicating higher stability of its crystal structure than that of S-ZFO.

*3.2. Vibrational Analysis.* The FTIR spectrum (Figure1b) indicated the formation of spinel ZFO, signifying a fundamental alteration in the material composition. The bands observed at 443 and 546 cm$^{-1}$ are attributed to the intrinsic stretching vibrations of Zn–O and Fe–O, respectively, which correspond to the tetrahedral and octahedral sites of spinel

ijer, 2025, 1, Downloaded from https://onlinelibrary.wiley.com/doi/10.1155/er/5520837 by Chung-Ang University, Seoul, Wiley Online Library on [06/05/2025]. See the Terms and Conditions (https://onlinelibrary.wiley.com/terms-and-conditions) on Wiley Online Library for rules of use; OA articles are governed by the applicable Creative Commons License

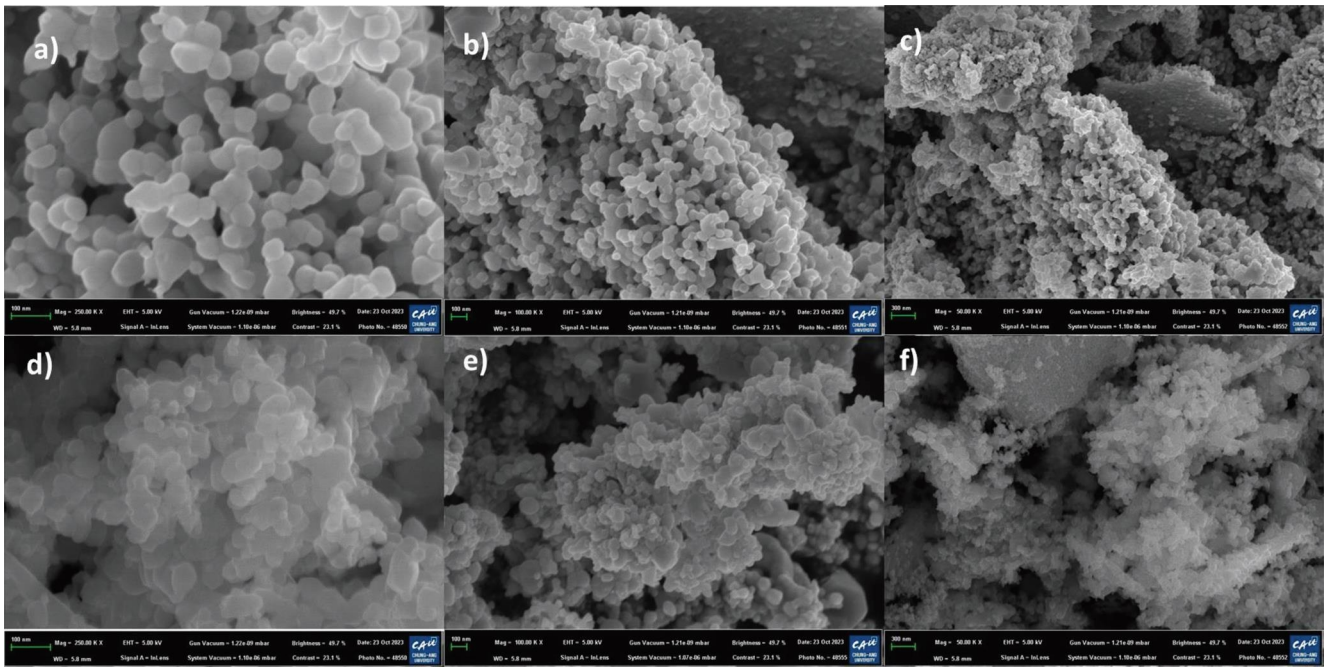



FIGURE 2: FESEM images of (a–c) IC-ZFO (hard-templated) and (d–f) S-ZFO (soft-templated) at different magnifications, highlighting the surface morphology, and agglomeration behavior of the materials.

ZFO [34, 35]. In the case of S-ZFO, these metal oxide vibration bands exhibited slight shifts to 447 and 548 $cm^{-1}$, indicating localized modification in ZFO. The bands at 3641 (IC-ZFO) and 3605 $cm^{-1}$ (S-ZFO) can be ascribed to –OH stretching vibrations owing to the presence of water molecules [36]. The peaks observed at 2879 and 2881 $cm^{-1}$ are due to the $–CH_2$ stretching bands of IC-ZFO and S-ZFO [37], respectively. The observation of minor band shifts in surfactant-incorporated spinel ZFO suggests that Triton X-100 coordinates with the metal surface via oxygen atoms.

*3.3. Morphological Analysis.* The morphology of S-ZFO and IC-ZFO was examined through FESEM; the corresponding images are presented in Figure 2. The image of IC-ZFO showed uniformly distributed spherical shapes, with grain sizes of ~30 nm (Figure 2a–c). S-ZFO was found to contain spherical grains, with sizes of ~40 nm, and undergo less agglomeration (Figure 2d–f). Furthermore, as ice crystals grow in the specific direction of hydrogen bonding between water molecules, this directed growth can potentially influence the nucleation and growth of ZFO nanoparticles, leading to less agglomeration and small, more uniform grains.

In addition, because Triton X-100 is a nonionic surfactant, it can adsorb onto the surface of the ZFO nanoparticles, creating a steric barrier that prevents agglomeration. Thus, the surfactant-assisted method may not be as effective as the ice-template method, which allows excellent directional growth and imparts porosity. The high efficiency of the ice crystal method for producing ZFO nanomaterials with optimized morphological characteristics makes it preferable to soft-template approaches. Figure 3 presents the TEM images and particle size distributions of IC-ZFO and S-ZFO. The TEM images reveal a spherical morphology for both the ZFO nanomaterials. The SAED patterns display structural fringes for both samples, underscoring their high crystallinity. Unlike S-ZFO, IC-ZFO exhibits well-defined spherical patterns in the TEM images. For IC-ZFO, represented in Figure 3a–d, the particles exhibit a relatively uniform distribution, with an average particle size ranging from 30 to 40 nm. The histogram in Figure 3d confirms the narrow distribution, which is indicative of a more consistent particle morphology. This uniformity contributes to improved lithium-ion diffusion pathways, enhancing overall electrochemical performance. In the case of S-ZFO, depicted in Figure 3e–h, it shows a broader particle size distribution, with an average particle size in the range of 40–50 nm. The histogram in Figure 3h demonstrates a wider spread in particle size compared to IC-ZFO, indicating less uniformity. Larger and less uniform particles in S-ZFO can hinder ion transport and reduce active surface area availability, which may negatively impact the materials energy storage performance. The comparative analysis of the particle size histograms (Figure 3d,h) underscores IC-ZFO's advantage in achieving better electrochemical properties due to its more uniform and smaller particle size distribution, making it a more promising candidate for LIB applications. Moreover, ice-template synthesis process three times under identical conditions. Each synthesis yielded ZFO particles with a consistent size of ~30 nm and minimal variation (±0.5 nm), demonstrating high reproducibility. These results confirm the robustness of the ice-template synthesis method and suitability for reuse, thereby supporting claims of commercial scalability and environmental sustainability.

*3.4. Elemental Analysis.* The chemical composition of IC-ZFO and S-ZFO was investigated through EDS with elemental mapping. Figure 4a,b shows the peaks associated with Fe,

ijer, 2025, 1, Downloaded from https://onlinelibrary.wiley.com/doi/10.1155/er/5320837 by Chung-Ang University, Seoul, Wiley Online Library on [06/05/2025]. See the Terms and Conditions (https://onlinelibrary.wiley.com/terms-and-conditions) on Wiley Online Library for rules of use; OA articles are governed by the applicable Creative Commons License

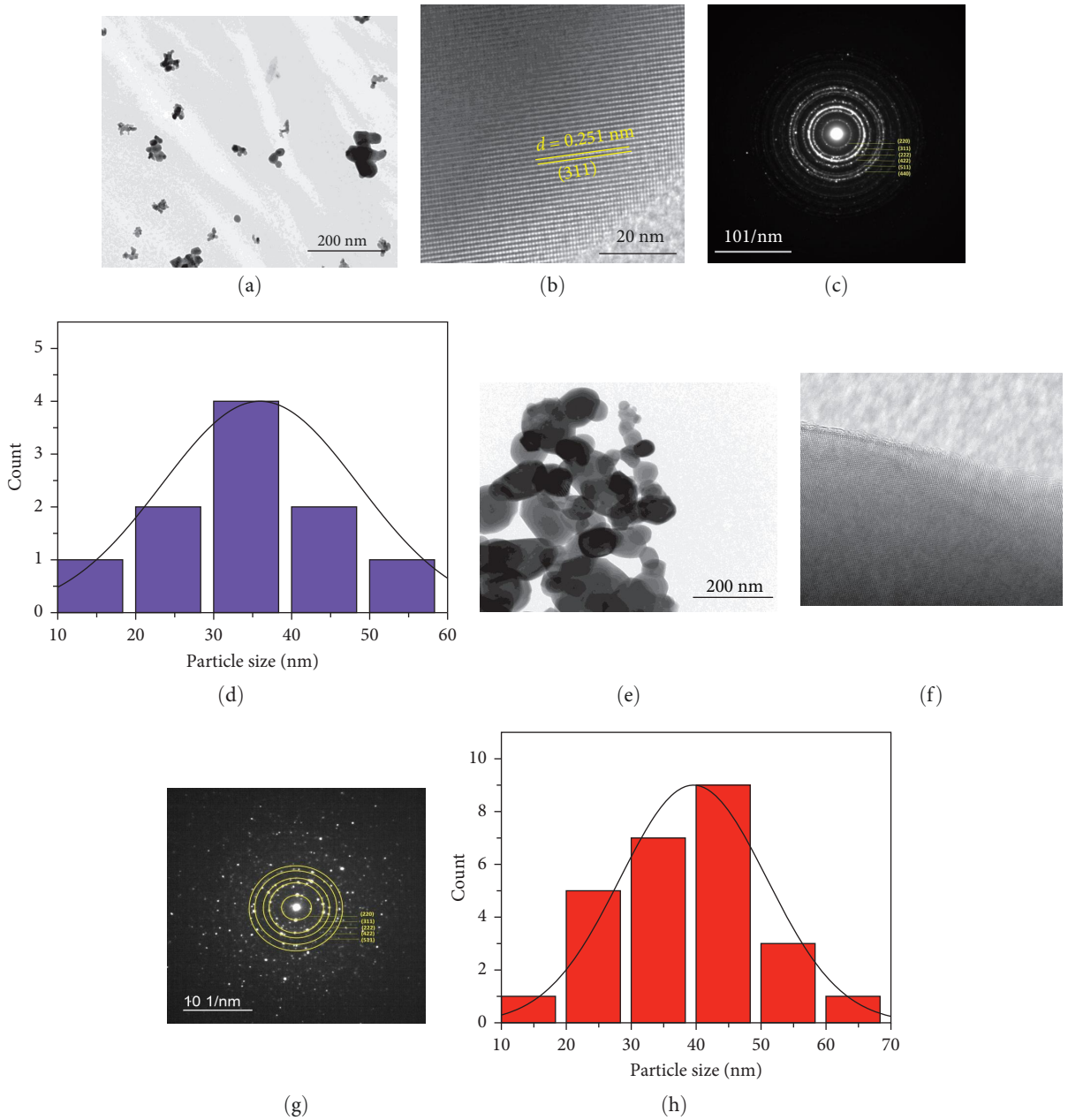



FIGURE 3: TEM images of (a, b) IC-ZFO and (e, f) S-ZFO. SAED patterns of (c) IC-ZFO and (g) S-ZFO; particle sizes of (d) IC-ZFO and (h) S-ZFO.

Zn, and O, indicating the precision of the synthesis process. Moreover, no traces of impurities were observed in the EDS results, confirming the high purity of the synthesized samples. The elemental mappings of the ZFO samples also demonstrate the uniform distribution of Zn, Fe, O, and C. The theoretical and resulting chemical compositions of the prepared ZFO material by both synthesis methods are shown in Table 2.

*3.5. BET Surface Area Analysis.* The specific surface area is a key factor influencing the storage capability of electrode materials, as it directly affects the availability of reaction sites [38, 39]. To evaluate the average particle size and surface area of the prepared zinc ferrite nanoparticles, BET surface area analysis was conducted for both IC-ZFO and S-ZFO. Figure 5 shows the BET surface area of prepared $ZnFe_2O_4$ nanomaterial by IC-ZFO and S-ZFO. The specific surface area was determined to be 6 $m^2/g$ for S-ZFO and 11 $m^2/g$ for IC-ZFO. Additionally, pore size analysis through the BJH method revealed pore diameters of 42 nm for S-ZFO and 61 nm for IC-ZFO (inset panel in Figure 5). The increased pore size in IC-ZFO may be attributed to its unique ice crystal synthesis method, which creates a more open and interconnected porous network. In contrast, the slightly lower surface area of IC-ZFO compared to S-ZFO could be explained by the denser arrangement of larger pores, leading to a reduced

ijer, 2025, 1, Downloaded from https://onlinelibrary.wiley.com/doi/10.1155/er/5520837 by Chung-Ang University, Seoul, Wiley Online Library on [06/05/2025]. See the Terms and Conditions (https://onlinelibrary.wiley.com/terms-and-conditions) on Wiley Online Library for rules of use; OA articles are governed by the applicable Creative Commons License

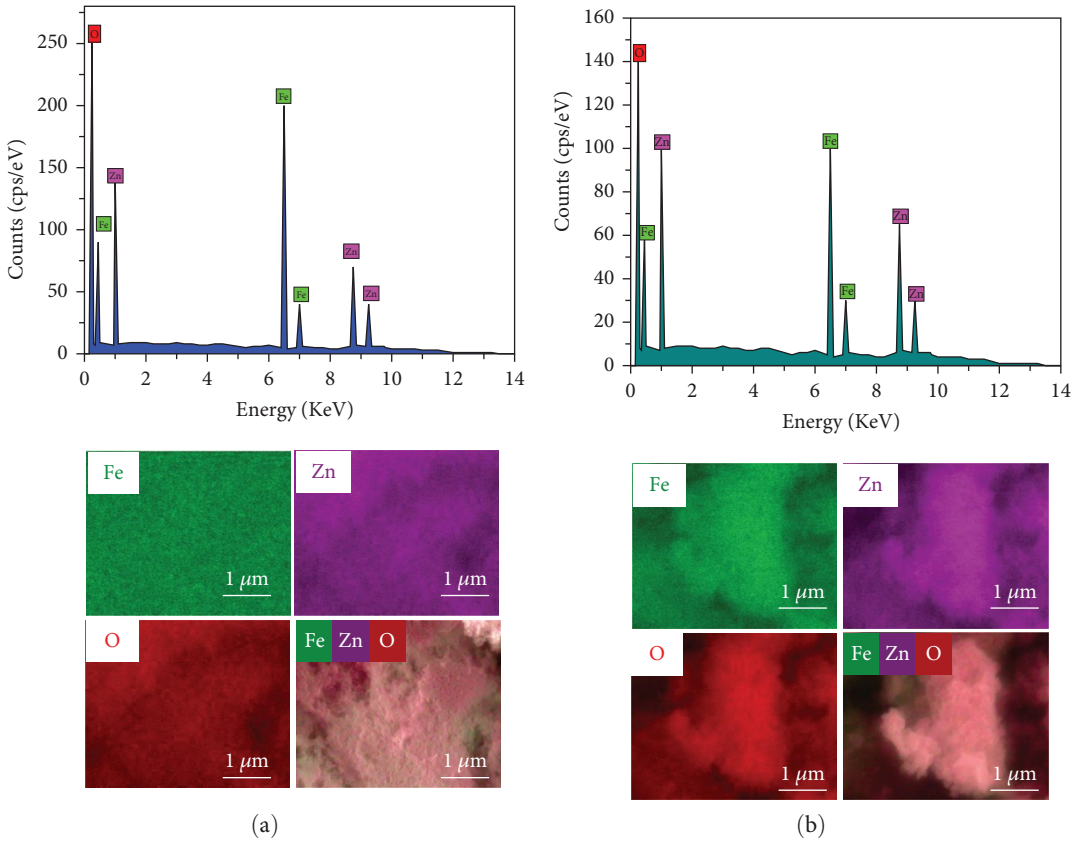



Figure 4: EDS spectra and mapping images of (a) IC-ZFO and (b) S-ZFO.

Table 2: Elemental composition of ZFO determined through EDS.

| Element | Theoretical (atomic wt.%) | Observed (atomic wt.%) | | Expected composition | Resultant composition | |
|---|---|---|---|---|---|---|
| | | IC-ZFO | S-ZFO | | IC-ZFO | S-ZFO |
| Zn | 14.28 | 14.40 | 14.01 | 1.00 | 1.00 | 0.98 |
| Fe | 28.57 | 28.97 | 27.28 | 2.00 | 2.02 | 1.90 |
| O | 57.14 | 56.64 | 58.11 | 4.00 | 3.96 | 4.06 |

total surface area contribution. The structural and surface characteristics of IC-ZFO and S-ZFO reveal distinct advantages and limitations for LIB applications. IC-ZFO, with a BET surface area of 11 $m^2$/g and a larger pore size of 61 nm, offers significant benefits in enhancing electrolyte penetration and reducing ion transport resistance, which facilitates faster lithium-ion intercalation and extraction. Its interconnected porous structure improves accessibility to active sites, contributing to better rate performance and capacity utilization. Additionally, the moderate surface area ensures sufficient active sites for lithium storage without compromising structural integrity during repeated charge–discharge cycles. On the other hand, S-ZFO, with a lower surface area of 6 $m^2$/g and a smaller pore size of 42 nm, exhibits a more compact structure that may limit ion mobility and diffusion, particularly under high-rate cycling conditions. The reduced surface area also restricts the availability of active sites, potentially leading to lower energy density compared to IC-ZFO. These differences highlight the superior performance potential of IC-ZFO for lithium-ion energy storage applications.

## 4. Electrochemical Studies

*4.1. Electrochemical Impedance Spectroscopy (EIS).* EIS of IC-ZFO and S-ZFO was conducted over frequencies ranging from 1 mHz to 100 kHz. In Figure 6, the Nyquist plots of both IC- and spinel S-ZFO reveal distinct features: a semicircle in the high-to-intermediate frequency range and a straight sloping line in the low-frequency range. The inset in Figure 6 depicts the corresponding equivalent circuit model, where $R_{ohm}$ represents the ohmic resistance, reflecting the combined resistance of the electrolyte, separator, and electrode. By analyzing the equivalent circuit, parameters such as electrolyte impedance ($R_1$), solid–electrolyte interface [27] impedance ($R_2$), charge transfer resistance ($R_3$), and constant phase element were derived (Figure 6). Interestingly, the

ijer, 2025, 1, Downloaded from https://onlinelibrary.wiley.com/doi/10.1155/er/5520837 by Chung-Ang University, Seoul, Wiley Online Library on [06/05/2025]. See the Terms and Conditions (https://onlinelibrary.wiley.com/terms-and-conditions) on Wiley Online Library for rules of use; OA articles are governed by the applicable Creative Commons License

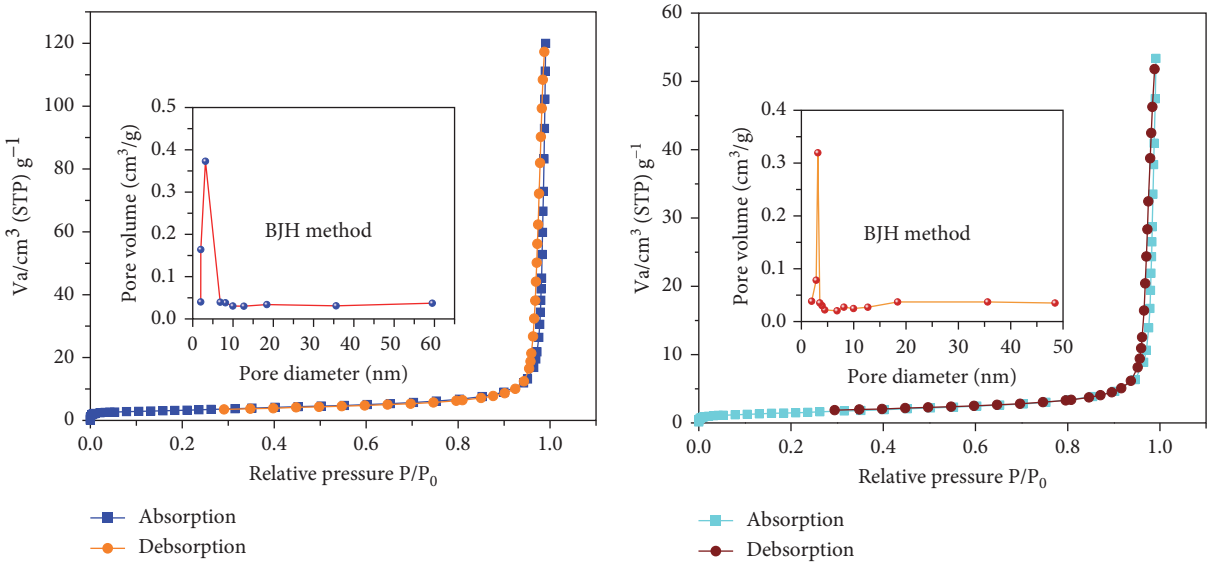



FIGURE 5: $N_2$ adsorption–desorption isotherms of (a) IC-ZFO and (b) S-ZFO nanoparticles. Insets in both panels illustrate the pore size distribution of the respective materials.

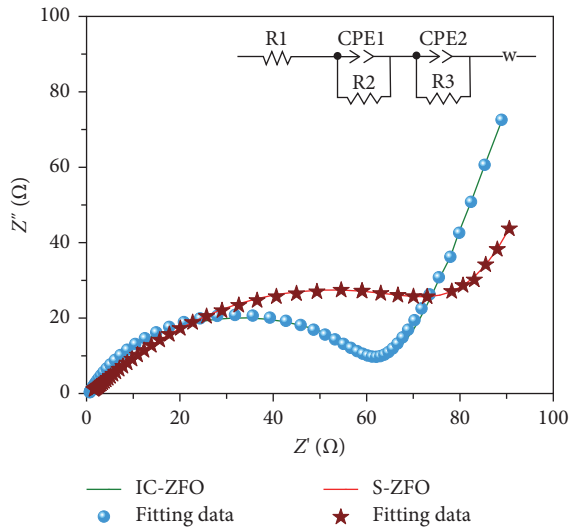



FIGURE 6: Nyquist plots of IC-ZFO and S-ZFO.

EIS profiles of all samples exhibited similar shapes, characterized by a semicircle in the high-to-medium-frequency region and a straight line in the low-frequency region. The impedance characteristics are primarily influenced by the surface morphology of electrode materials and are proportional to the diameter of the semicircle in the Nyquist plot. The first semicircle in the high-frequency region indicates the presence of the SEI layer [38]. The charge transfer reactions occurring at the electrolyte–electrode interface contribute to $R_3$, which is represented by the second semicircle in the middle-frequency region. Additionally, $Li^+$ diffusion within the electrode materials is attributable for the sloping line observed in the low-frequency region [40].

Notably, when as the anode material, IC-ZFO anode demonstrated lower resistance than S-ZFO, as observed from the EIS results. The lower resistance of IC-ZFO is likely due to the differences in the surface morphology of the two nanomaterials (Figure 2). Morphological studies revealed that ice crystal-assisted synthesis produces smaller, more uniformly distributed particles, which enhance electrochemical performance. In contrast, the soft-template method produces large particle sizes and promotes agglomeration, which reduce the effective surface area and increase in resistance. Variances in the synthesis methods can affect the $Li^+$ diffusion kinetics, resulting in impedance behavior differences. In addition, compliance with causality, linearity, and stability in impedance measurements was ensured through residual or error analysis, and the impedance fit parameters followed the Kramers–Kronig (K–K) relationship [18, 41]. The error analysis plots for IC-ZFO and S-ZFO, covering the real and imaginary impedance values over the measured frequency range, demonstrated conformity with these principles, confirming the reliability of the measurements (Figure 7). The K–K relations ensure consistency between the real and imaginary parts of a complex function, verifying the accuracy of experimental data. This method helps identify errors and uncertainties, ensuring measurements comply with the principles of causality and linearity, particularly in frequency-dependent systems [32]. Figure 7 shows the relative error between the real and imaginary parts of the measured impedance ($Z_{real}$, $Z_{imag}$) and the calculated values ($Z_{calc}$) across 0–80 Hz. Figure 7a,b demonstrates minimal deviations at lower frequencies, indicating strong conformity with the K–K relationship. Figure 7c,d shows slight deviations at higher frequencies, likely due to instrumental noise or polarization effects, but these do not impact the overall interpretation of the material's electrochemical performance. These results confirm that the impedance data accurately

ijer, 2025, 1, Downloaded from https://onlinelibrary.wiley.com/doi/10.1155/er/5520837 by Chung-Ang University, Seoul, Wiley Online Library on [06/05/2025]. See the Terms and Conditions (https://onlinelibrary.wiley.com/terms-and-conditions) on Wiley Online Library for rules of use; OA articles are governed by the applicable Creative Commons License

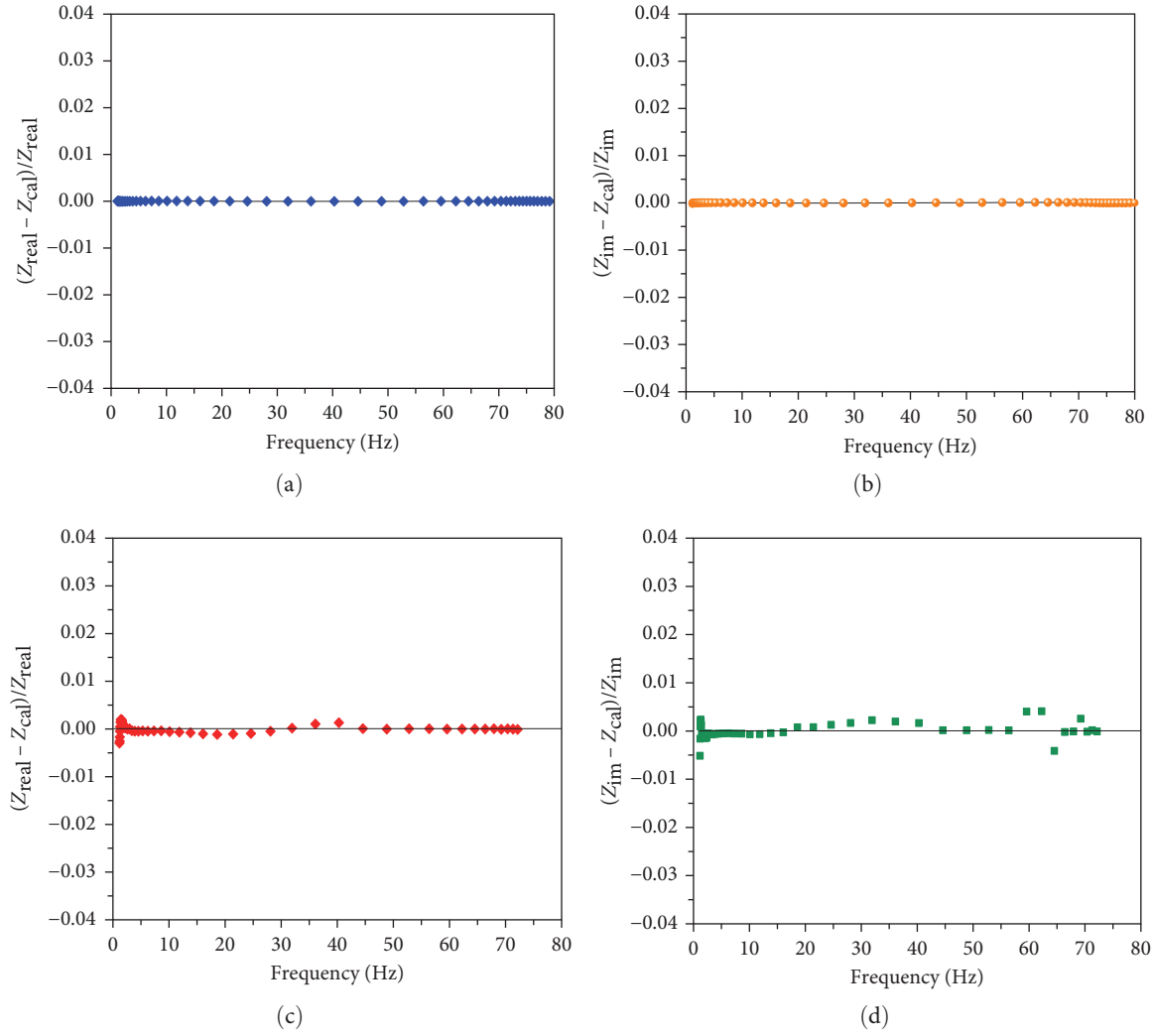



FIGURE 7: Error analysis for (a) real ($Z$) versus frequency; (b) imaginary [41] versus frequency of IC-ZFO; (c) real ($Z$) versus frequency; and (d) imaginary [41] versus frequency of S-ZFO.

reflect the electrochemical properties of the systems and that the fit parameters derived from the experimental data are reliable.

*4.2. CV.* The CV was conducted to investigate the lithiation and delithiation behaviors of the spinel ZFO nanocomposite electrodes. Figure 8a illustrates the initial CV curves of the ZFO samples at a scan rate of 10 mV $s^{-1}$ over a voltage range of 0.01–3.0 V. The CV curves of the samples indicate a consistent intercalation–deintercalation process of $Li^+$ ions. In Figure 8a for IC-ZFO, a distinct peak is observed during the initial cathodic scan of the first cycle, attributed to the irreversible reduction reaction with the electrolyte, at 0.77 V. This reduction peak corresponds to the irreversible reduction of $Fe^{3+}$ to $Fe^0$ and $Zn^{2+}$ to $Zn^0$, which is associated with the formation of $Li_2O$ and the Li-Zn alloy [36, 42–44]. Moreover, the prominent reduction peaks centered at 0.92 and 0.77 V persist in the subsequent cathodic scans at scan rates of 10–100 mV $s^{-1}$ (Figure 8b). During the anodic scan, peaks at 1.7 V are observed, indicating the oxidation of $Zn^0$ and $Fe^0$ to $Fe_2O_3$ and ZnO, respectively.

Similarly, in Figure 8a, for S-ZFO, reduction peaks are observed at 0.77 V, indicating the conversion of ZFO to Li ions. The anodic scan displays peaks at 1.7 V, as well as a new oxidation peak at 2.41 V, potentially linked to the oxidation of $Fe_2O_3$ to $Fe^0$ and ZnO to $Zn^0$, respectively [39]. Furthermore, oxidation peak emerges at 2.41 V, suggesting further oxidation occurs within the electrode material. These oxidation peaks signify crucial transformations that occur during the anodic phase of the cycling process, potentially influencing the overall electrochemical performance and stability of the electrode. Upon cycling, the cathodic peaks disappear and are replaced by new peaks at 1.1 and 0.97 V (Figure 8c), indicating the reversible reduction of $Fe_2O_3$ to $Fe^0$ and ZnO to $Zn^0$, respectively. Therefore, the anodic peaks exhibit a slight shift to 1.7 and 1.85 V in the subsequent cycles, observed at scan rates of 10–100 mV $s^{-1}$.

Notably, a significant observation emerged for both IC-ZFO and S-ZFO: the cathodic and anodic peaks exhibited substantial overlap from the second scan onward, confirming the outstanding reversible electrochemical performance. Moreover, the persistence of these cathodic and anodic peaks

ijer, 2025, 1, Downloaded from https://onlinelibrary.wiley.com/doi/10.1155/er/5520837 by Chung-Ang University, Seoul, Wiley Online Library on [06/05/2025]. See the Terms and Conditions (https://onlinelibrary.wiley.com/terms-and-conditions) on Wiley Online Library for rules of use; OA articles are governed by the applicable Creative Commons License

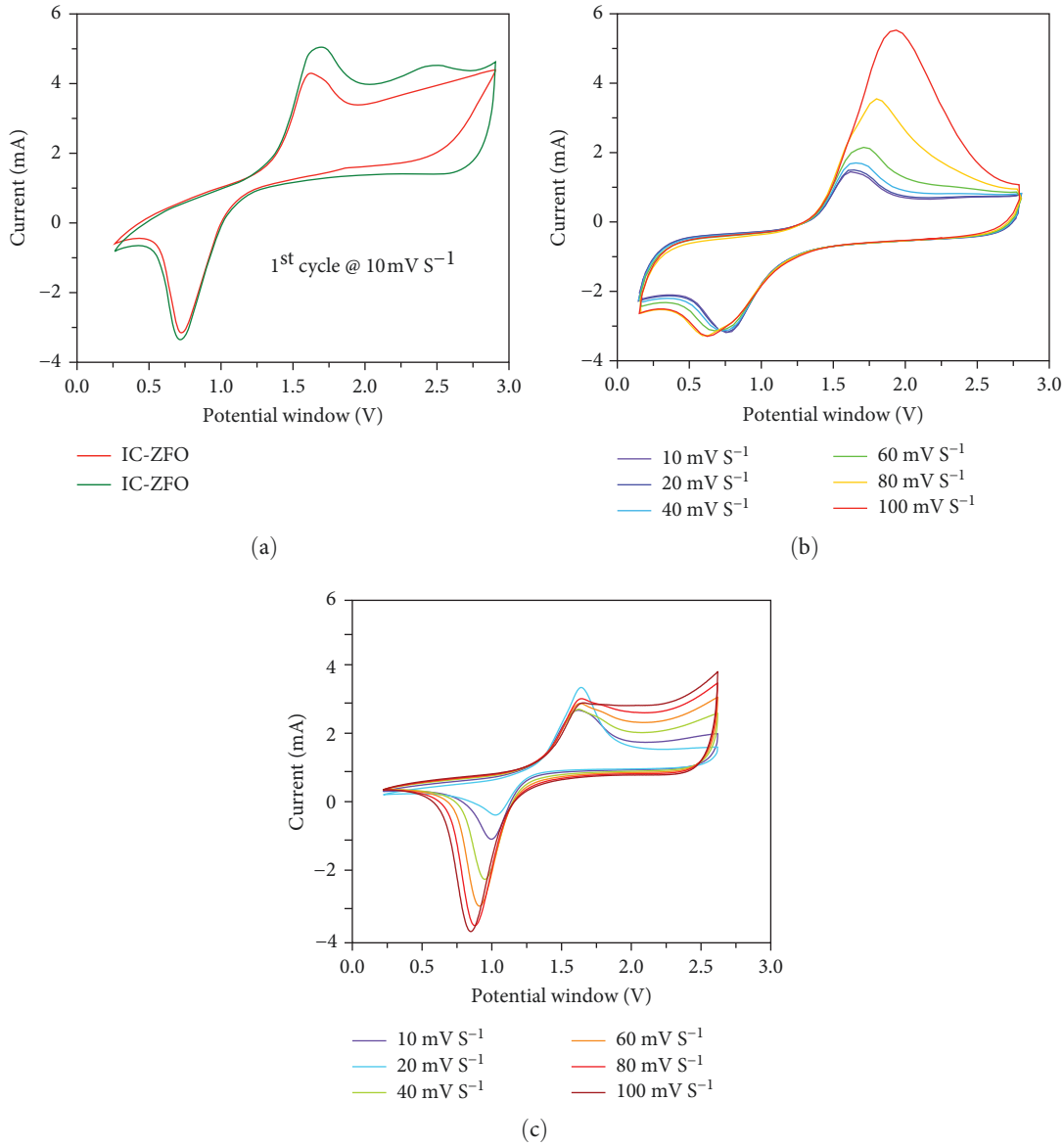



FIGURE 8: CV curves: (a) 1st cycle at 10 mV $s^{-1}$, (b) IC-ZFO, and (c) S-ZFO at different scan rates.

underscores the excellent stability and reversibility of the ZFO anodes. Furthermore, the shapes of the CV curves remained largely consistent at different scan rates, with minimal shifts observed in the oxidation and reduction peaks, suggesting weak electrochemical polarization. The effect of different scan rates (10–100 mV/s) on the reaction kinetics and reversibility shows that at higher scan rates, polarization increases, leading to broader peaks and higher current densities, while at lower scan rates, the reaction becomes more reversible with sharper peaks. The consistent shape of the CV curves indicates stable electrochemical behavior, but peak shifts and separation suggest changes in kinetics [45]. These results imply excellent electrochemical stability and performance of the electrode materials. The morphology and structure of $ZnFe_2O_4$ nanoparticles are critical for their lithium-ion storage and electrochemical performance. Smaller, uniformly sized nanoparticles increase surface area, enabling faster charge/discharge rates, minimizing diffusion resistance, and enhancing rate capability and cycling stability. A well-defined crystalline structure further improves electronic conductivity and charge transfer [35].

Based on the CV observations and previously reported results [46], the lithium-ion storage mechanisms for the entire electrochemical reaction are proposed as follows:

$$ZnFe_2O_4 + 0.5Li^+ + 0.5e^- \rightarrow Li_{0.5}ZnFe_2O_4, \quad (1)$$

$$Li_{0.5}ZnFe_2O_4 + 1.5Li^+ + 1.5e^- \rightarrow Li_2ZnFe_2O_4, \quad (2)$$

$$Li_2ZnFe_2O_4 + 6Li^+ + 6e^- \rightarrow 4Li_2O + Zn + 2Fe, \quad (3)$$

$$Zn + Li^+ + e^- \leftrightarrow LiZn\,(\text{alloy}), \quad (4)$$

$$3Li_2O + 2Fe \leftrightarrow Fe_2O_3 + 6Li^+ + 6e^-, \quad (5)$$

ijer, 2025, 1, Downloaded from https://onlinelibrary.wiley.com/doi/10.1155/er/5520837 by Chung-Ang University, Seoul, Wiley Online Library on [06/05/2025]. See the Terms and Conditions (https://onlinelibrary.wiley.com/terms-and-conditions) on Wiley Online Library for rules of use; OA articles are governed by the applicable Creative Commons License

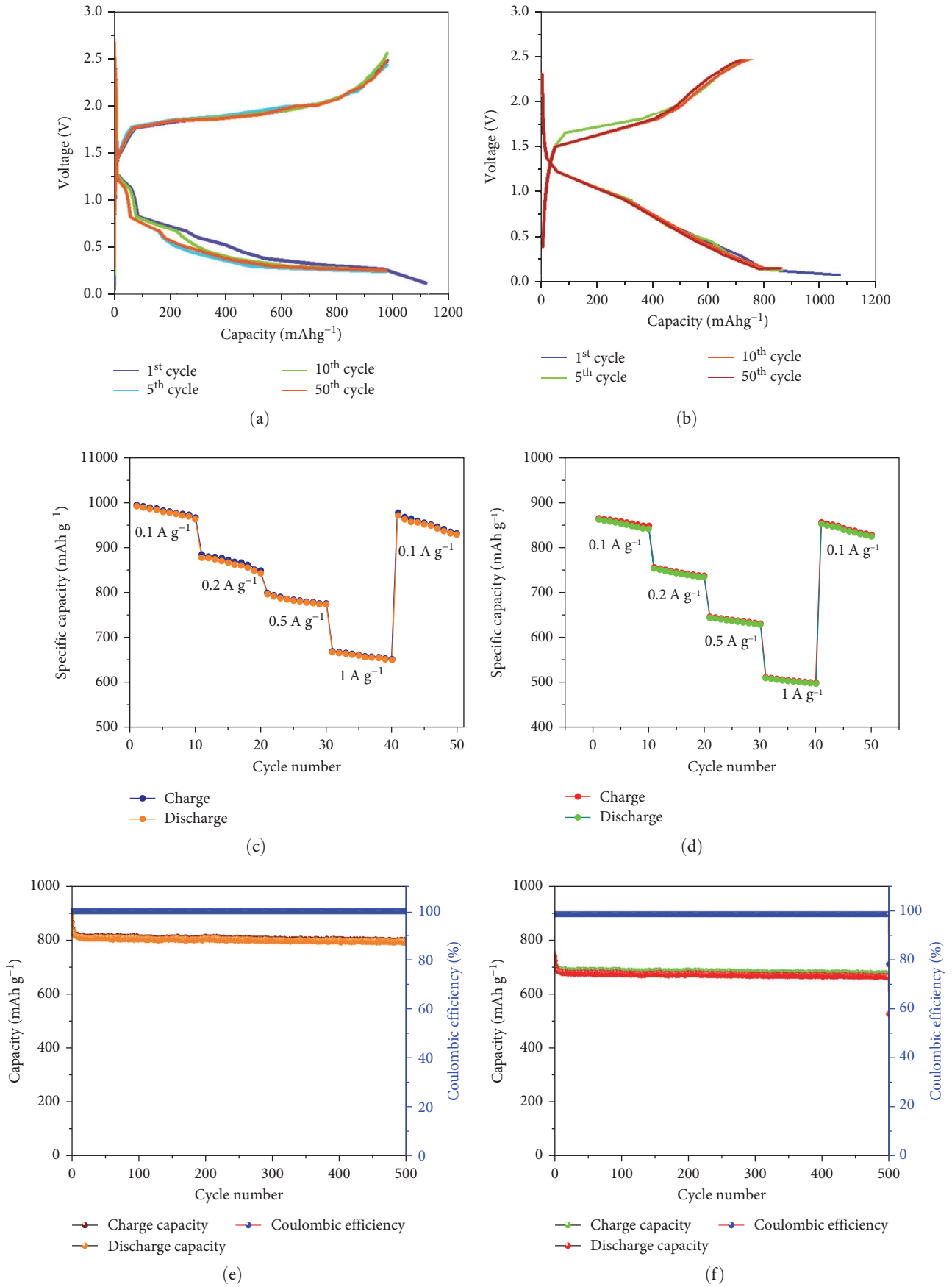



FIGURE 9: Discharge–charge profiles for the selected cycles: (a) IC-ZFO and (b) S-ZFO. Rate capability at various current densities: (c) IC-ZFO and (d) S-ZFO. Cycling performance and Coulombic efficiency: (e) IC-ZFO and (f) S-ZFO.

ijer, 2025, 1, Downloaded from https://onlinelibrary.wiley.com/doi/10.1155/er/5520837 by Chung-Ang University, Seoul, Wiley Online Library on [06/05/2025]. See the Terms and Conditions (https://onlinelibrary.wiley.com/terms-and-conditions) on Wiley Online Library for rules of use; OA articles are governed by the applicable Creative Commons License

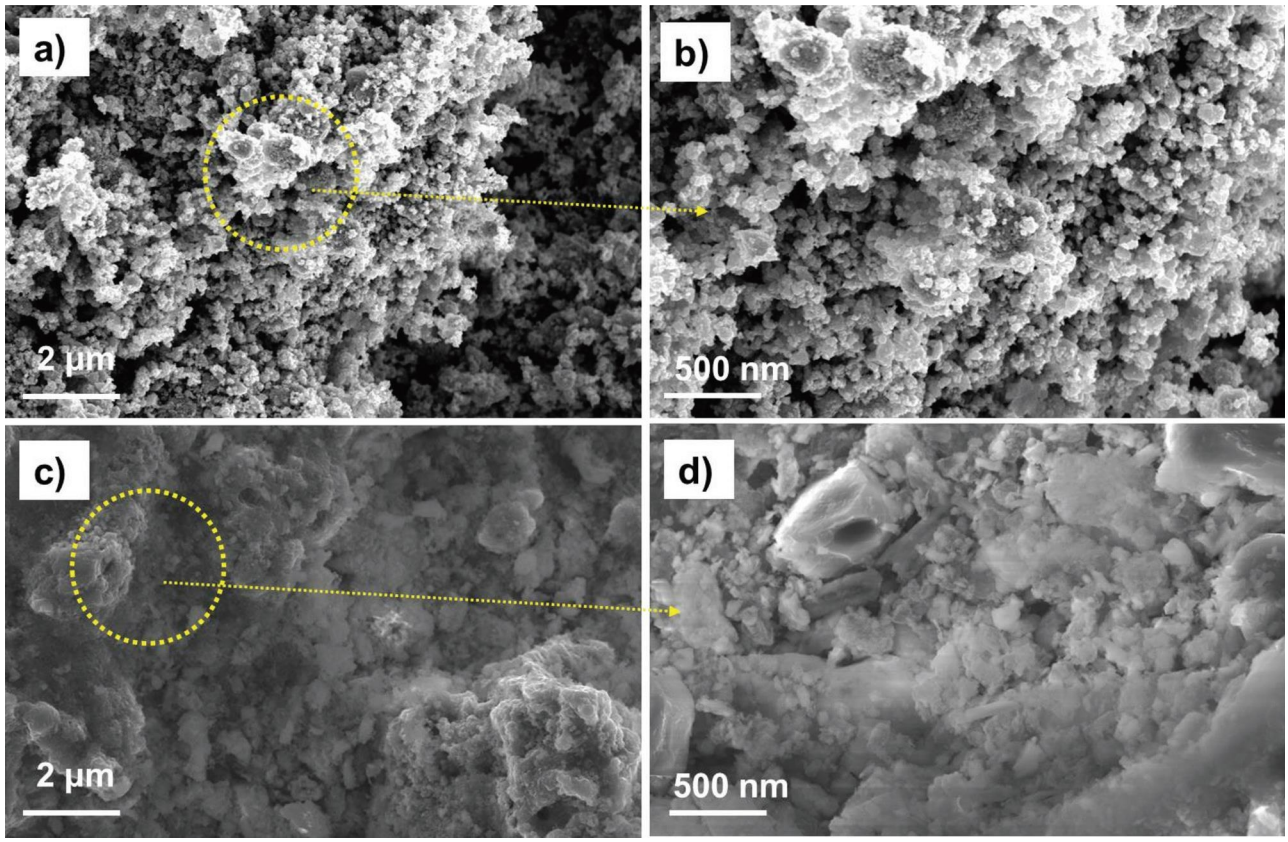



FIGURE 10: FESEM image of (a, b) IC-ZFO and (c, d) S-ZFO nanoparticles after 500 cycles.

$$Li_2O + Zn \leftrightarrow ZnO + 2Li^+ + 2e^-. \quad (6)$$

*4.3. Charge and Discharge.* Figure 9a,b illustrates the discharge and charge profiles for selected cycles of the electrodes at a current density of 0.1 A $g^{-1}$ within a potential voltage window of 0–3.0 V at room temperature (27°C). The discharge and charge voltage plateaus correspond with the CV results. The first discharge curve exhibits two distinct plateaus, a short one at 0.96 V and a long one at 0.80 V, which becomes less pronounced in the subsequent discharge profiles. The former plateau is attributed to the formation of $Li_xZnFe_2O_4$ (Equation 1), whereas the latter is linked to the decomposition of ZFO into $Zn^0$ and $Fe^0$ dispersed in the $Li_2O$ matrix (Equation 2) [39, 46]. Additionally, $Zn^0$ nanoparticles undergo alloying reactions with Li beyond the plateau region to form a Li-Zn alloy (Equation 3) [44]. Upon reaching 0.01 V, IC-ZFO and S-ZFO deliver an initial discharge capacity of ~1128 and 1087 mAh $g^{-1}$, respectively. Excess capacity beyond the theoretical specific capacity may result from the storage capacity of the interfacial SEI layer. The first charge curve displays a smooth, increasing trend with a plateau voltage at 1.74 V, attributed to the dealloying reaction and reversible conversion reaction for the formation of $Fe_2O_3$ and ZnO. After the first cycle, the discharge and charge capacities gradually increase slightly before declining with further cycling; this process is referred to as electrolyte activation. The subsequent discharge and charge processes exhibit overlapping curves with ultrahigh Coulombic efficiencies, indicating excellent stable cycling performance (over 99.6% for IC-ZFO and 98.2% for S-ZFO).

To determine the differences in the electrochemical properties of the two electrodes, the rate capacities of IC-ZFO and S-ZFO were examined at different current densities, as shown in Figure 9c,d. The IC-ZFO nanomaterial demonstrates decent lithiation capacity retention, with average discharge capacities of 980 ($5^{th}$), 865 ($15^{th}$), 798 ($25^{th}$), 657 mAh $g^{-1}$ ($35^{th}$), 581 mAh $g^{-1}$ ($45^{th}$), and 403 mAh $g^{-1}$ ($55^{th}$) at current densities of 0.1, 0.2, 0.5, 1, 2, and 5 A $g^{-1}$, respectively. A high average discharge capacity of 951mAh $g^{-1}$ is achieved when the current density returns to 0.1 mAh $g^{-1}$. For the S-ZFO material, lithiation capacity retention exhibits average discharge capacities of 855 ($5^{th}$), 742 ($15^{th}$), 636 ($25^{th}$), 503 mAh $g^{-1}$ ($35^{th}$), 402 mAh $g^{-1}$ ($45^{th}$), and 285 mAh $g^{-1}$ ($55^{th}$) at current densities of 0.1, 0.2, 0.5, 1, 2, and 5 A $g^{-1}$, respectively. Subsequently, a high average discharge capacity of 839 mAh $g^{-1}$ is observed when the current density returns to 1 A $g^{-1}$.

To further underscore the high cycling stability, long-term cycling performance of both ZFO anode materials was analyzed at a current of 0.5 Ah $g^{-1}$ for 500 cycles. IC-ZFO maintained a stable capacity with high Coulombic efficiency after 500 cycles, as shown in Figure 9e. The discharge and charge capacities of IC-ZFO remained at 797 and 793 mAh $g^{-1}$, respectively, throughout the 500 cycles, with 99.4% capacity retention. Daoyan Feng et al. [37] reported 3D hierarchically porous $ZnFe_2O_4$/C composites with excellent electrochemical performance, delivering 711 mAh $g^{-1}$ at

ijer, 2025, 1, Downloaded from https://onlinelibrary.wiley.com/doi/10.1155/er/5520837 by Chung-Ang University, Seoul, Wiley Online Library on [06/05/2025]. See the Terms and Conditions (https://onlinelibrary.wiley.com/terms-and-conditions) on Wiley Online Library for rules of use; OA articles are governed by the applicable Creative Commons License

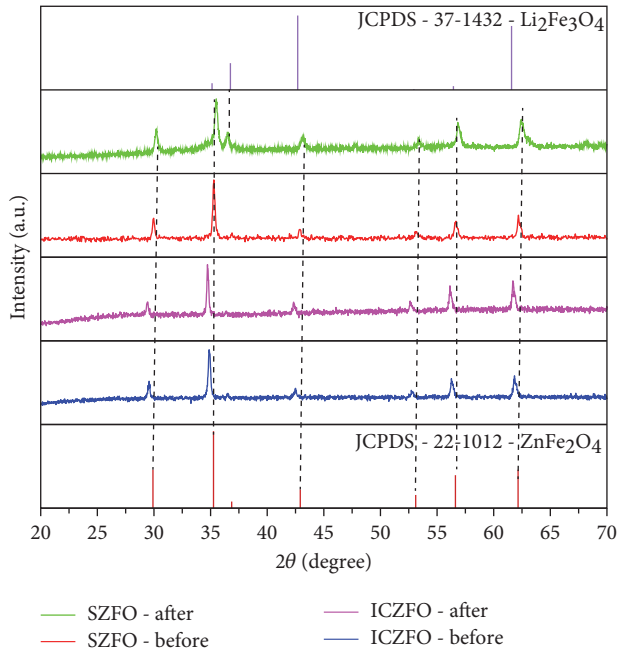



FIGURE 11: XRD patterns of $ZnFe_2O_4$ nanoparticles by hard-templated and soft-templated method after 500 cycles (the standard XRD patterns of cubic $ZnFe_2O_4$ and cubic $Li_2Fe_3O_4$ are also shown for reference).

1000 mA $g^{-1}$ after 400 cycles, showcasing their potential for high-performance LIBs. Lin et al. developed core–shell structured $ZnFe_2O_4$@C nanoparticles, and it delivered a reversible capacity of 705 mAh $g^{-1}$ at 0.25 C after 180 cycles [47, 48]. Compared to other results, IC-ZFO exhibited better electrochemical performance. Ice-template $ZnFe_2O_4$, with spherical morphology, offers a high surface area for abundant lithium-ion insertion sites, enhancing capacity and rate performance. Its controlled structure ensures cycling stability by reducing mechanical stress, while the well framework morphology improves electron conduction and reduces polarization. These features make it a promising material for high-performance LIBs [23]. Similarly, as shown in Figure 9f, the discharge and charge capacities of S-ZFO remained stable at 674 and 625 mAh $g^{-1}$, respectively, over 500 cycles, with 92.7% capacity retention. Moreover, the Coulombic efficiency, an important electrochemical parameter, particularly in lithium-ion full cells, of IC-ZFO and S-ZFO significantly improved and gradually reached ~99.6% and 98.2% during the subsequent cycles. Figure 10 shows the FESEM image of the $ZnFe_2O_4$ anode material after 500 charging and discharging cycles of the IC-ZFO and S-ZFO. This result indicates the excellent electrochemical reversibility of the ZFO anode during cycling. Figure 10 shows the structural evolution of IC-ZFO and S-ZFO anodes after 500 cycles at a current density of 500 mA $g^{-1}$ was analyzed using FESEM, as shown in Figure 10 a,b which depicts IC-ZFO at low and high magnifications, while Figure 10c,d represents S-ZFO at similar magnifications. After 500 cycles, IC-ZFO largely retains its structural morphology, with the nanoparticles remaining well interconnected and showing minimal changes (Figure 10a,b). At higher magnification (Figure 10b), some degree of agglomeration is observed, but the overall structure remains intact, indicating good stability under prolonged cycling. In the case of S-ZFO, more pronounced agglomeration is evident (Figure 10c,d), with a noticeable loss of the distinct nanoparticle structure observed before cycling. At higher magnification (Figure 10), the particles appear significantly fused together, with increased irregularity and fragmentation, suggesting reduced mechanical stability compared to IC-ZFO. These results highlight IC-ZFO's ability to maintain structural integrity after extensive cycling, while S-ZFO shows more substantial agglomeration and structural deterioration, making IC-ZFO a more suitable material for long-term LIB applications. Figure 11 shows the XRD patterns of IC-ZFO, and S-ZFO anode reveals stark differences in structural stability and their subsequent impact on electrochemical performance over prolonged cycling. The IC-ZFO demonstrates notable structural integrity, with its XRD patterns remaining consistent even after 500 charge–discharge cycles. This stability directly correlates with ability to sustain consistent electrochemical performance over long cycle. The absence of new diffraction peaks in IC-ZFO confirms minimal or negligible structural transformations during lithium intercalation and deintercalation processes, so preserving electrochemical activity and ensuring superior cycling stability. On the other hand, S-ZFO exhibits a significant structural transformation upon cycling, as evidenced by the emergence of a new peak in XRD pattern corresponding to cubic $Li_2Fe_3O_4$ (JCPDS card No. 37-1432). This indicates that S-ZFO exhibits a phase transition during lithium intercalation. While the initial electrochemical performance has been satisfactory, the structural changes lead to a gradual degradation of the spinel framework, resulting in capacity fading and diminished long-term performance. The formation of the $Li_2Fe_3O_4$ phase is indicative of irreversible structural changes that compromise the material stability and

ijer, 2025, 1, Downloaded from https://onlinelibrary.wiley.com/doi/10.1155/er/5520837 by Chung-Ang University, Seoul, Wiley Online Library on [06/05/2025]. See the Terms and Conditions (https://onlinelibrary.wiley.com/terms-and-conditions) on Wiley Online Library for rules of use; OA articles are governed by the applicable Creative Commons License

Table 3: Particle size and electrochemical performance of ZFO obtained through various synthesis routes.

| Synthesis method | Particle size (nm) | Discharge capacity (mAh $g^{-1}$) | Capacity retention | Refs. |
|---|---|---|---|---|
| Green synthesis | 35 | 350 | 75.5% after 100 cycles | [38] |
| Hydrothermal | 40 | 450 | 80.5% after 300 cycles | [40] |
| Coprecipitation | 50 | 811 | 82% after 250 cycles | [41] |
| Sol–gel | 30–40 | 456 | 79% after 600 cycles | [42] |
| Solvothermal | 5–10 | 519 | 71% after 300 cycles | [43] |
| Spray analysis | — | 753 | 75.2% after 200 cycles | [44] |
| Ice-template synthesis | 30 | 991 | 89.30% after 500 cycles | Present work |

electrochemical reliability. From the postcycling, XRD analysis highlights the critical role of structural integrity in determining cycling performance. The exceptional cycling stability of IC-ZFO anode material from its resistance to structural degradation makes it a strong candidate for long-term energy storage applications. Conversely, the phase instability in S-ZFO underlines the necessity for structural optimization to moderate performance fading, emphasizing the importance of stability in designing durable energy storage materials. Moreover, ZFO prepared through ice-template synthesis exhibited high electrochemical performance than those through other synthesis methods (Table 3).

## 5. Conclusions

ZFO nanoparticles were synthesized using both a rapid ice-template synthesis method (IC-ZFO) and a sol–gel method (S-ZFO) incorporating a soft-template (Triton X-100). The electrochemical properties of these materials were analyzed, and their applicability as anode materials in LIBs was verified. Both IC-ZFO and S-ZFO exhibited excellent capacity retention, achieving ~99.6% and 98.2% Coulombic efficiencies, respectively. IC-ZFO demonstrated a discharge/charge capacity of 797/793 mAh $g^{-1}$ with a Coulombic efficiency of 99.4% over 500 cycles. In comparison, S-ZFO exhibited an initial discharge/charge capacity of 674/625 mAh $g^{-1}$ with a Coulombic efficiency of 92.7% over 500 cycles. The electrochemical performance of ZFO is attributed to its continuous structural framework and uniform surface morphology, facilitating reversible lithiation/delithiation processes. IC-ZFO, in particular, had a uniform morphology and small crystallite and particle sizes, which were realized without using surfactants. This uniform morphology, likely due to the ice crystal template method, enhanced the electrochemical performance of IC-ZFO because of the availability of a large surface area for efficient charge transfer and ion diffusion during cycling. In contrast to chemical templates like Triton X-100, which utilize surfactants and pose environmental concerns due to the challenges in their removal, ice crystals serve as a natural, biodegradable, and reusable alternative, making the synthesis process more sustainable. Additionally, the ice-template process avoids the use of harmful chemicals, minimizes waste, and supports sustainable synthesis practices. This approach aligns with the growing emphasis on green chemistry and sustainable material development, adding depth and significance to the study. This proposed method is a cost-effective and rapid approach for designing spinel ZFO structures with abundant voids and improved morphology and is suitable for the development of high-performance electrodes for LIBs.

## Data Availability Statement

All data generated or analyzed during this study are included in this published article.

## Conflicts of Interest

The authors declare no conflicts of interest.

## Funding

This study was supported by the National Research Foundation of Korea (grant number RS-2024-00413272). Dr. Devaraj Lakshmi acknowledges PSG College of Arts and Science for providing SEED grant (IRSG/2023-2024/Physics/010).

## References

[1] D. Lakshmi, M. Infanta Diana, B. Nalini, et al., "Fine-Tuning of Stannic Oxide Anodes' Material Properties Through Calcination," *Journal of Materials Science: Materials in Electronics* 32 (2021): 27384–27397.

[2] H. Li, Z. Wang, L. Chen, and X. Huang, "Research on Advanced Materials for Li-Ion Batteries," *Advanced Materials* 21 (2009): 4593–4607.

[3] A. S. Arico, P. Bruce, B. Scrosati, J.-M. Tarascon, and W. Van Schalkwijk, "Nanostructured Materials for Advanced Energy Conversion and Storage Devices," *Nature Materials* 4, no. 5 (2005): 366–377.

[4] M. Salah, P. Murphy, C. Hall, C. Francis, R. Kerr, and M. Fabretto, "Pure Silicon Thin-Film Anodes for Lithium-Ion Batteries: A Review," *Journal of Power Sources* 414 (2019): 48–67.

[5] D. Lakshmi, M. I. Diana, G. Manoj, et al., "Influence of Reducing Agents in Nanoparticle Synthesis: $SnO_2$-ZnO Composite Anode," *Applied Organometallic Chemistry* 36 (2022).

[6] S. Fang, D. Bresser, and S. Passerini, "Transition Metal Oxide Anodes for Electrochemical Energy Storage in Lithium-and Sodium-Ion Batteries," *Transition Metal Oxides for Electrochemical Energy Storage* (2022): 55–99.

[7] M. Ahmad, T. Nawaz, X. Chen, et al., "Binder-Free Ni-Doped In/Mn Oxalate Electrode for Next-Generation Supercapacitors," *International Journal of Hydrogen Energy* 83 (2024): 1113–1119.

[8] L. Devaraj, J. S, N. Balakrishnan, and P. Christopher Selvin, "Compound Semiconducting SnSb Alloy Anodes for Li Ion Batteries: Effect of Elemental Composition of Sn-Sb," *Semiconductor Science and Technology* (2020).

ijer, 2025, 1, Downloaded from https://onlinelibrary.wiley.com/doi/10.1155/er/5520837 by Chung-Ang University, Seoul, Wiley Online Library on [06/05/2025]. See the Terms and Conditions (https://onlinelibrary.wiley.com/terms-and-conditions) on Wiley Online Library for rules of use; OA articles are governed by the applicable Creative Commons License

[9] P. Sivaraj, B. Nalini, K. P. Abhilash, D. Lakshmi, P. Christopher Selvin, and P. Balraju, "Study on the Influences of Calcination Temperature on Structure and Its Electrochemical Performance of $Li_2FeSiO_4$/C Nano Cathode for Lithium Ion Batteries," *Journal of Alloys and Compounds* 740 (2018): 1116–1124.

[10] M. Ahmad, T. Nawaz, I. Hussain, et al., "Situ Synthesis of Oriented Zn-Mn-Co-Telluride on Precursor Free CuO: An Experimental and Theoretical Study of Hybrid Electrode Paradigm for Advanced Supercapacitors," *Nano Materials Science* (2024).

[11] P. Perumal, T. Kiruthika, P. Sivaraj, D. Lakshmi, and P. C. Selvin, "Tamarind Seed Polysaccharide Biopolymer-Assisted Synthesis of Spinel Zinc Iron Oxide as A Promising Alternate Anode Material for Lithium-Ion Batteries," *Journal of Materials Science: Materials in Electronics* 31 (2020): 10593–10604.

[12] X. Yang, H. Wang, Y. Song, et al., "Low-Temperature Synthesis of a Porous High-Entropy Transition-Metal Oxide as An Anode for High-Performance Lithium-Ion Batteries," (ACS Appl Mater Interfaces (2022).

[13] Z. Zuhra, M. H. Khan, S. Ali, M. Ahmad, and Z. Zhaowei, "Metal-Organic Frameworks for Sustainable Precious Metal Recovery: A Review of Recent Advances," *Chemical Engineering Journal* (2024): 157105.

[14] M. Bini, M. Ambrosetti, and D. Spada, "$ZnFe_2O_4$, a Green and High-Capacity Anode Material for Lithium-Ion Batteries," *A Review, Applied Sciences* 11 (2021).

[15] Z. Zuhra, M. Ahmad, Y. Abbas, S. Ali, S. Li, I. Hussain, G. Xie, X. Wang, Role of Heteroatoms (N, P, "O, and S) in $Co_3O_4$-Doped Carbons Derived from ZIF-67-Polyphosphazene Nanohybrids as Anode Materials for Supercapacitors," *ACS Applied Nano Materials* 6 (2023): 18045–18053.

[16] X. Guo, X. Lu, X. Fang, et al., "Lithium Storage in Hollow Spherical $ZnFe_2O_4$ as Anode Materials for Lithium Ion Batteries," *Electrochemistry Communications* 12 (2010): 847–850.

[17] P. Poizot, S. Laruelle, S. Grugeon, L. Dupont, and J. M. Tarascon, "Nano-Sized Transition-Metal Oxides as Negative-Electrode Materials for Lithium-Ion Batteries," *Nature* 407, no. 6803 (2000): 496–499.

[18] D. Lakshmi and B. Nalini, "Performance of SnSb: Ce, Co Alloy as Anode For Lithium-Ion Batteries," *J. Solid State Electrochem* 21 (2016): 1027–1034.

[19] P. Makkar and N. N. Ghosh, "Facile Synthesis of $MnFe_2O_4$ Hollow Sphere-Reduced Graphene Oxide Nanocomposites as Electrode Materials for All-Solid-State Flexible High-Performance Asymmetric Supercapacitors," *ACS Applied Energy Materials* 3 (2020): 2653–2664.

[20] D. D. Andhare, S. A. Jadhav, M. V. Khedkar, S. B. Somvanshi, S. D. More, and K. M. Jadhav, "Structural and Chemical Properties of $ZnFe_2O_4$ Nanoparticles Synthesised by Chemical Co-Precipitation Technique," *Journal of Physics: Conference Series* 1644 (2020): 012014.

[21] F. Iqbal, M. I. A. Mutalib, M. S. Shaharun, M. khan, and B. Abdullah, "Synthesis of $ZnFe_2O_4$ Using Sol-Gel Method: Effect of Different Calcination Parameters," *Procedia Engineering* 148 (2016): 787–794.

[22] D. K. Narale, P. D. Kumbhar, R. R. Bhosale, et al., "Rational Design of Binder Free $NiFe_2O_4$@$CoFe_2O_4$ Core-Shell Nanoflake Arrays Synthesized by Chemical Bath Deposition for Supercapacitor Application," *Journal of Energy Storage* 66 (2023).

[23] M. Shaterian, A. Rezvani, and A R, "Abbasian, Controlled Synthesis and Self-Assembly of $ZnFe_2O_4$ Nanoparticles Into Microspheres by Solvothermal Method," *Materials Research Express* 6 (2020).

[24] L. Lv, Y. Wang, P. Cheng, B. Zhang, F. Dang, and L. Xu, "Ultrasonic Spray Pyrolysis Synthesis Of Three-Dimensional $ZnFe_2O_4$-Based Macroporous Spheres for Excellent Sensitive Acetone Gas Sensor," *Sensors Actuators B: Chem* 297 (2019).

[25] M. M. Vadiyar, S. S. Kolekar, J.-Y. Chang, A. A. Kashale, and A. V. Ghule, "Reflux Condensation Mediated Deposition of $Co_3O_4$ Nanosheets and $ZnFe_2O_4$ Nanoflakes Electrodes for Flexible Asymmetric Supercapacitor," *Electrochimica Acta* 222 (2016): 1604–1615.

[26] T. Guo, M.-S. Yao, Y.-H. Lin, and C.-W. Nan, "A Comprehensive Review on Synthesis Methods for Transition-Metal Oxide Nanostructures," *CrystEngComm* 17 (2015): 3551–3585.

[27] J. A. Kumar, T. Krithiga, S. Manigandan, et al., "A Focus to Green Synthesis of Metal/Metal Based Oxide Nanoparticles," *Various Mechanisms and Applications Towards Ecological Approach. Journal of Cleaner Production* 324 (2021): 129198.

[28] C. Jin, Y. Lu, G. Tong, R. Che, and H. Xu, "Excellent Microwave Absorbing Properties of ZnO/$ZnFe_2O_4$/Fe Core-Shell Microrods Prepared by a Rapid Microwave-Assisted Hydrothermal-Chemical Vapor Decomposition Method," *Applied Surface Science* 531 (2020).

[29] A. K. Rai, S. Kim, J. Gim, M. H. Alfaruqi, V. Mathew, and J. Kim, "Electrochemical Lithium Storage of a $ZnFe_2O_4$/Graphene Nanocomposite as An Anode Material for Rechargeable Lithium Ion Batteries," *RSC Advances* 4 (2014): 47087–47095.

[30] Y. Park, M. Oh, and J. H. Kim, "Well-Dispersed $ZnFe_2O_4$ Nanoparticles Onto Graphene as Superior Anode Materials for Lithium Ion Batteries," *Energies* 12 (2019): 304.

[31] S. B. Bandgar, M. M. Vadiyar, C. L. Jambhale, J.-H. Kim, and S. S. Kolekar, "Superfast Ice Crystal-Assisted Synthesis of $NiFe_2O_4$ and $ZnFe_2O_4$ Nanostructures for Flexible High-Energy Density Asymmetric Supercapacitors," *Journal of Alloys and Compounds* 853 (2021): 157129.

[32] S. E. Shirsath, M. L. Mane, Y. Yasukawa, X. Liu, and A. Morisako, "Self-Ignited High Temperature Synthesis and Enhanced Super-Exchange Interactions of Ho(3+)-Mn(2+)-Fe(3+)-O(2-) Ferromagnetic Nanoparticles," *Physical Chemistry Chemical Physics* 16 (2014): 2347–2357.

[33] Y. Ding, Y. Yang, and H. Shao, "High Capacity $ZnFe_2O_4$ Anode Material for Lithium Ion Batteries," *Electrochimica Acta* 56 (2011): 9433–9438.

[34] E. Sarala, M. Madhukara Naik, M. Vinuth, Y. V. Rami Reddy, and H. R. Sujatha, "Green Synthesis of Lawsonia Inermis-Mediated Zinc Ferrite Nanoparticles for Magnetic Studies and Anticancer Activity Against Breast Cancer (MCF-7) Cell Lines," *Journal of Materials Science: Materials in Electronics* 31 (2020): 8589–8596.

[35] M. Mandal, S. Subudhi, I. Alam, et al., "Facile Synthesis of New Hybrid Electrode Material Based on Activated Carbon/Multiwalled Carbon Nanotubes@ZnFe2O4 for Supercapacitor Applications," *Inorganic Chemistry Communications* 123 (2021).

[36] W. Yao, Z. Xu, X. Xu, et al., "Two-Dimensional Holey $ZnFe_2O_4$ Nanosheet/Reduced Graphene Oxide Hybrids by Self-Link of Nanoparticles for High-Rate Lithium Storage," *Electrochimica Acta* 292 (2018): 390–398.

[37] T. Yang, W. Zhang, L. Li, et al., "In-Situ Synthesized $ZnFe_2O_4$ FIRMLY Anchored to the Surface of MWCNTs As A Long-Life Anode Material With High Lithium Storage Performance," *Applied Surface Science* 425 (2017): 978–987.

ijer, 2025, 1, Downloaded from https://onlinelibrary.wiley.com/doi/10.1155/er/5320837 by Chung-Ang University, Seoul, Wiley Online Library on [06/05/2025]. See the Terms and Conditions (https://onlinelibrary.wiley.com/terms-and-conditions) on Wiley Online Library for rules of use; OA articles are governed by the applicable Creative Commons License

[38] D. Bresser, E. Paillard, R. Kloepsch, et al., "Carbon Coated $ZnFe_2O_4$ Nanoparticles for Advanced Lithium-Ion Anodes," *Advanced Energy Materials* 3 (2012): 513–523.
[39] M. Zhang, Y. Liu, H. Zhu, and X. Wang, "Hierarchical Bead Chain $ZnFe_2O_4$-PEDOT Composites With Enhanced Li-Ion Storage Properties as Anode Materials for Lithium-Ion Batteries," *Applied Surface Science* 529 (2020).
[40] H. Liu, W. Tang, M. Zhang, and X. Sun, "Microstructure Construction of Pearl Necklace Like Structured $Fe_3O_4$/MWCNT Composites for Li-Ion Battery," *Journal of Nanoelectronics and Optoelectronics* 16 (2021): 343–350.
[41] M. Kasper, A. Leike, J. Thielmann, C. Winkler, N. Al-Zubaidi R-Smith, and F. Kienberger, "Electrochemical Impedance Spectroscopy Error Analysis and Round Robin On Dummy Cells and Lithium-Ion-Batteries," *Journal of Power Sources* 536 (2022).
[42] C. M. Park, J. H. Kim, H. Kim, and H. J. Sohn, "Li-Alloy Based Anode Materials for Li Secondary Batteries," *Chemical Society Reviews* 39, no. 8 (2010): 3115–3141.
[43] D. Feng, H. Yang, and X. Guo, "3-Dimensional Hierarchically Porous $ZnFe_2O_4$/C Composites With Stable Performance as Anode Materials for Li-Ion Batteries," *Chemical Engineering Journal* 355 (2019): 687–696.
[44] X. Yang, H. Xue, Q. Yang, R. Yuan, W. Kang, and C.-S. Lee, "Preparation of Porous ZnO/$ZnFe_2O_4$ Composite From Metal Organic Frameworks and Its Applications for Lithium Ion Batteries," *Chemical Engineering Journal* 308 (2017): 340–346.
[45] Y. Gao, L. Yin, S. J. Kim, et al., "Enhanced Lithium Storage by $ZnFe_2O_4$ Nanofibers as Anode Materials for Lithium-Ion Battery," *Electrochimica Acta* 296 (2019): 565–574.
[46] M. W. Alam, A. BaQais, M. M. Rahman, et al., "Investigation on In Situ Carbon-Coated ZnFe(2)O(4) as Advanced Anode Material for Li-Ion Batteries," *Gels* 8 (2022).
[47] L. Lin and Q. Pan, "$ZnFe_2O_4$@ C/Graphene Nanocomposites as Excellent Anode Materials for Lithium Batteries," *Journal of Materials Chemistry A* 3 (2015): 1724–1729.
[48] R. Roshani and A. Tadjarodi, "Synthesis of $ZnFe_2O_4$ Nanoparticles With High Specific Surface Area for High-Performance Supercapacitor," *Journal of Materials Science: Materials in Electronics* 31 (2020): 23025–23036.

ijer, 2025, 1, Downloaded from https://onlinelibrary.wiley.com/doi/10.1155/er/5520837 by Chung-Ang University, Seoul, Wiley Online Library on [06/05/2025]. See the Terms and Conditions (https://onlinelibrary.wiley.com/terms-and-conditions) on Wiley Online Library for rules of use; OA articles are governed by the applicable Creative Commons License